International Journal of Nanoelectronics and Materials
Volume 16 January 2023 [121-134]

Effect of Various Carbon Coating Techniques on the Electrochemical Performance of $Li_4Ti_5O_{12}$ Synthesized by Sol-Gel Method

Slamet Priyono[1,2], Jan Setiawan[2], Wahyu Bambang Widayatno[2], and Akhmad Herman Yuwono[1]

[1]Department of Metallurgical and Materials Engineering, Faculty of Engineering, Universitas Indonesia, Depok 16424, Indonesia
[2]National Research and Innovation Agency, Tangerang Selatan 15310, Indonesia

Received 3 March 2022, Revised 21 May 2022, Accepted 20 July 2022

ABSTRACT

This study aimed to prepare spinel carbon-coated $Li_4Ti_5O_{12}$ (LTO/C) via sol-gel reaction and applied as a high-performance lithium-ion battery anode. The LTO powder was coated using various carbon sources, super P (SP), sugar and PVDF-assisted SP. The crystal structure, morphology, conductivity and electrochemical performance of the samples were examined using X-ray diffraction (XRD), Field Emission scanning electron microscopy (FESEM), Fourier Transform Infrared (FTIR) spectroscopy, Electrochemical Impedance Spectroscopy (EIS) and Cyclic Voltammetry/Charge-discharge (CV/CD), respectively. The XRD analysis results showed that the samples contain highly crystalline spinel LTO as the main phase and rutile as impurity. The FESEM image showed that SP covers the entire LTO surface more homogenous than sugar. However, sugar carbon makes roughness on the LTO surface. FTIR spectra showed that the coating using sugar and PVDF still contain hydrocarbon element. Electrochemical performance evaluations showed that SP carbon-coated-LTO possesses higher lithium diffusion and specific capacity than pure LTO, while sugar-coated-LTO shows the lowest specific capacity. Moreover, the SP carbon-coated-LTO sample high-rate capability has improved during full cell evaluation, delivering a discharge capacity of 249, 231, 211, 194, 58, and 23 $mAhg^{-1}$ at the charge or discharge current density of 0.05, 0.1, 0.5, 1, 5, and 10 C, respectively.

Keywords: Carbon-coated, $Li_4Ti_5O_{12}$, PVDF, sugar, Super P

1. INTRODUCTION

Lithium titanate or $Li_4Ti_5O_{12}$ (LTO) could substitute graphite as a negative electrode in the lithium-ion battery due to its high working potential of 1.55 V (vs. Li/Li^+). Its higher volumetric energy, power density and longer cycle life are suitable for future energy storage applications in electric vehicles, with less pollution and better safety [1, 2]. Since LTO exhibits volumetric stability during the charge-discharge process, it is considered a zero-strain material potentially useful at high C-rates while maintaining superior performance [3]. However, LTO has intrinsic kinetics limitations owing to its low electronics conductivity of 10^{-13} Sm^{-1} because of a wideband gap of 2 eV and poor Li^+ ion diffusion coefficient of 10^{-9} – 10^{-13} cm^2 s^{-1}. Consequently, it yields low capacities and high electrode polarization during intercalation and de-intercalation [4, 5]. Another challenge is direct contact between the LTO and electrolyte leads to the decomposition of electrolyte, resulting in a considerable amount of gas during charge-discharge process especially at elevated temperatures [6].

Several works have been proposed to solve the above-mentioned problems by coating using various materials including oxides [7], metal [8] and carbon [9]. Among these materials, carbon is considered as the most promising material for coating on the LTO due to its simple, effective,

and facile strategy that can increase electrical conductivity and Li^+ diffusion [6]. Carbon coating could be a conductive network that decreases the contact resistance amongst LTO particles [10]. Since carbon is permeable material to lithium diffusion, Li^+ ions easily move in and out of the active material. Although carbon coating decreases the energy density by forming solid electrolyte interphase (SEI) [11, 12], it helps avoid direct contact between active material and electrolyte and suppresses gas formation [13]. Therefore, carbon coating is the best method to improve the rate and cycle capability of materials [14] because it partially transforms Ti^{4+} into Ti^{3+} and enhances the ionic conductivity of LTO.

Carbon coating could be introduced as a post-treatment after synthesizing LTO or giving it during the phase formation of LTO. The first strategy controls carbon coating thickness on the LTO surface, though it is costly and less efficient. In contrast, the second strategy is more effective since the carbon coating, and LTO is heat-treated simultaneously [12, 15]. The carbon coating could be obtained in forms such as reduced graphene [16], carbon nanotubes [17], carbon fibers [18], amorphous carbon [19] and organic carbon sources [20]. Different carbon forms give various electrochemical performances of LTO anode, such as capacity, rate capability, or cycling stability [2, 21]. Carbon coating on the LTO surface is the most challenging problem for mass industrial anode production, particularly due to controlling the carbon thickness and uniformity [10, 22]. Although it is powerful, thicker carbon coating might restrict ion transport [23] and prevent particle growth [24]. Super P (SP) is a conductive carbon which potentially used for coating, while sugar as organic source and easy to attach on surface is very attractive to be used as a carbon source. PVDF or polyvinylidene fluoride, commonly used as a binder, is the polymer that suitable to increase the adhesion of carbon onto the LTO. This study aimed to determine the best carbon for coating on the LTO surface and significantly enhance LTO performance. This study utilized the carbon sources of Commercial Super P products, sugar, and SP assisted by PVDF with pyrolyzing methods.

2. MATERIAL AND METHODS

2.1 Materials

LTO powder was synthesized using lithium acetate (CH_3COOLi) and titanium butoxide ($C_{12}H_{28}O_4Ti$) as Li and Ti sources, respectively. Ethanol and HCl were used as a solvent and a catalyst, respectively. All materials were 99.99% pure and supplied by Sigma Aldrich. Super P as a carbon source for coating was supplied by MTI Corp China, while sugar as an organic carbon source was obtained from a grocery, and PVDF was purchased from Lin Yi Gelon.

2.2 Synthesis

2.2.1 Pure $Li_4Ti_5O_{12}$ (LTO) Synthesis

Pure LTO was synthesized using a sol-gel technique following the stoichiometry equation:

$$CH_3COOLi\ (s) + C_{12}H_{28}O_4Ti\ (l) \rightarrow Li_4Ti_5O_{12} \quad (1)$$

Lithium acetate powder (CH_3COOLi) and titanium butoxide ($C_{12}H_{28}O_4Ti$) were diluted in the ethanol solution with HCl as a catalyst. The lithium acetate solution was added into titanium butoxide drop-wise and stirred for 12 hours. The final solution was oven-dried at 80 ^oC for 24 hours and sintered at 850 ^oC in an air atmosphere for 4 hours to obtain white LTO powder. This first sample was denoted as Pure LTO sample.

2.2.2 Carbon Coated-LTO Synthesis

The second and third samples were carried out by the following procedure. About 10 wt% of super P and sugar were added into the as-sintered Pure LTO powder and denoted as LTO/SP and LTO/Sugar, respectively. The mixtures were ball-milled using planetary ball milling (PBM) at a speed of 20 Hz for 2 hours. The samples were then transferred into an alumina boat and sintered again under a nitrogen atmosphere at 600 ^{o}C for 2 hours. The fourth sample was prepared by mixing the pure sample into a slurry form using PVDF as a binder and super-P as a carbon source at a ratio of 85: 5: 10, respectively. The slurry was oven-dried at 80 ^{o}C for 24 h and sintered again under a nitrogen atmosphere at 600 ^{o}C for 2 hours. This sample was denoted by LTO/SP+PVDF as LTO coated PVDF-assisted SP. After sintering, all samples were pulverized using mortar and pestle and classified using a test sieve of 400 mesh.

2.3 Material Characterization

The sample crystals' structure and phases were determined using powder X-ray diffraction (XRD, Rigaku Smartlab 3kW Ser. No BD63000224-01) with Cu-Kα radiation sources (λ=0.154 nm) ranging from 10 to 90^{o} and step size of 0.01^{o}. The lattice parameter was obtained using Rietveld refinement. Furthermore, the crystallite sizes were approximately determined d by the W-H equation from the XRD pattern. The sample texture, morphology, and particle size were analyzed using scanning electron microscopy (FESEM, Hitachi SU-3500). Samples were tested using Fourier Transform Infra-Red (FTIR, Nicolet™iS™10) to get information about functional grub.

2.4 Electrochemical Characterization

The electrodes were fabricated by mixing the active material, carbon black, and binder at the ratio of 80:10:10 in N, N-Dimethylacetamide to get slurry mixture, which was subsequently coated on a Cu foil. The coin cells were prepared using an electrode, separator (Celgard), electrolyte ($LiPF_6$), and metal Li, and assembled in a glove box filled with Argon UHP. The impedance was characterized using electrochemical impedance spectroscopy (EIS) with the frequency of 1 MHz to 0.1 Hz and an AC signal amplitude of 5 mV. The cyclic voltammetry (CV) and charge-discharge (CD) profiles were evaluated using an automatic battery testing system (WBCS 3000). The CV test was conducted using a sweep voltage of 0.8 to 2.8 V (vs. Li+/Li) at a scan rate of 0.05, 0.1, 0.15, 0.2, 0.25, and 0.5 mVs^{-1}. The samples' specific capacity was calculated using the result of the CD test performed using the constant current (CC) method and were recorded between 0 - 3 V at 0.05, 0.1, 0.5, 1, 5, and 10C.

3. RESULTS AND DISCUSSION

3.1 Crystal Structure and Morphology Particle

The X-ray diffraction patterns of pristine and modified LTO are depicted in Figure 1. All samples possess high and sharp diffraction peaks and are indexed based on a cubic spinel LTO and the rutile tetragonal structure. The small reflections at 27.6^{o}, 36.1^{o} and 54.5^{o}, marked with an asterisk, belong to the rutile phase attributed to impurity. The rutile phase comes from transforming the anatase phase at 700-800 ^{o}C [14]. Carbon coating using different sources as a precursor does not change LTO's spinel structure, a result comparably consistent with LTO carbon coating using solid-state reaction [12]. The LTO planes of (111), (113), (004), (133), (115), (044), (135), (026), (226), (444) and (155) correspond with peaks at 18.4^{o}, 35.6^{o}, 43.3^{o}, 47.4^{o}, 57.3^{o}, 62.9^{o}, 66.1^{o}, 74.4^{o}, 75.4^{o}, 79.4^{o} and 82.4^{o}, respectively. Rietveld's refinement concluded that the LTO phase has structural parameters listed in Table 1. The small portion of rutile improves the electrochemical performances of cells owing to its high lithium diffusion coefficient [25]. Other studies found that nanocoating of rutile on the LTO highly improves density, stability, and

cycle ability [26]. Furthermore, carbon coating improves the crystallinity of LTO and reduces the rutile phase simultaneously, owing to the secondary heat treatment [27]. The data show that LTO/SP gives the highest improvement of the LTO phase. Also, Figure 2 shows the enlarged (111) peaks of LTO and rutile for better observation. It shows that the (111) peak increases while the rutile peak decreases after introducing carbon on the LTO surface, implying an increase in LTO crystallinity. The crystallinity is beneficial for electrochemical performance because an open channel within the LTO crystal structure facilitates lithium-ion migration along the b axis [28].

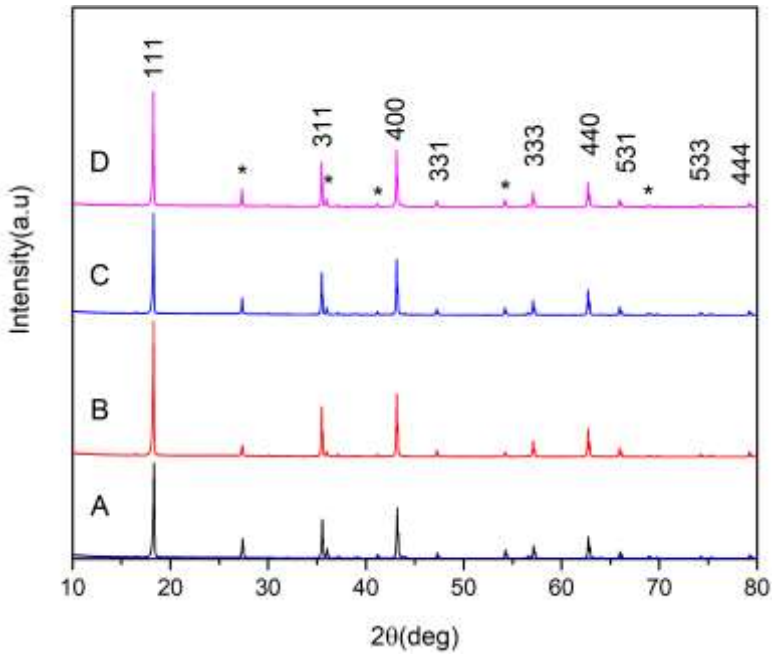

Figure 1. XRD patterns of: (A) Pure LTO, (B) LTO/SP, (C) LTO/Sugar, (D) LTO/SP+PVDF.

Table 1 Results of phase composition and structural parameters from the Rietveld analysis

Sample	LTO (%)	TiO2 (%)	Lattice parameter (Å)	Crystallite Size (nm)	Rp	Rwp	X^2
Pure LTO	84	16	8.3693	53	0.10	0.13	2.84
LTO/SP	92	8	8.3678	198	0.09	0.13	2.60
LTO/Sugar	89	11	8.3671	77	0.10	0.12	2.56
LTO/SP+PVDF	86	14	8.3656	87	0.09	0.12	2.62

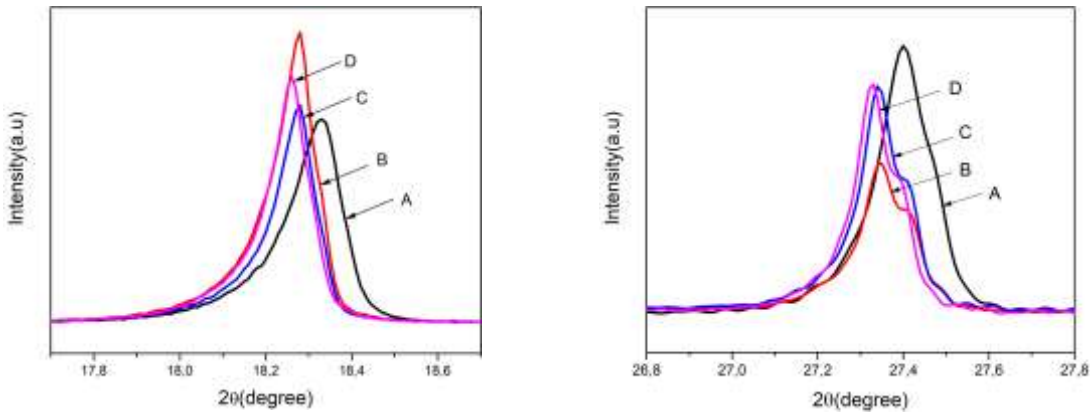

Figure 2. Detailed observation of [111] peak of LTO (left) and rutile (right) for: (A) Pure LTO, (B) LTO/SP, (C) LTO/Sugar, (D) LTO/SP+PVDF.

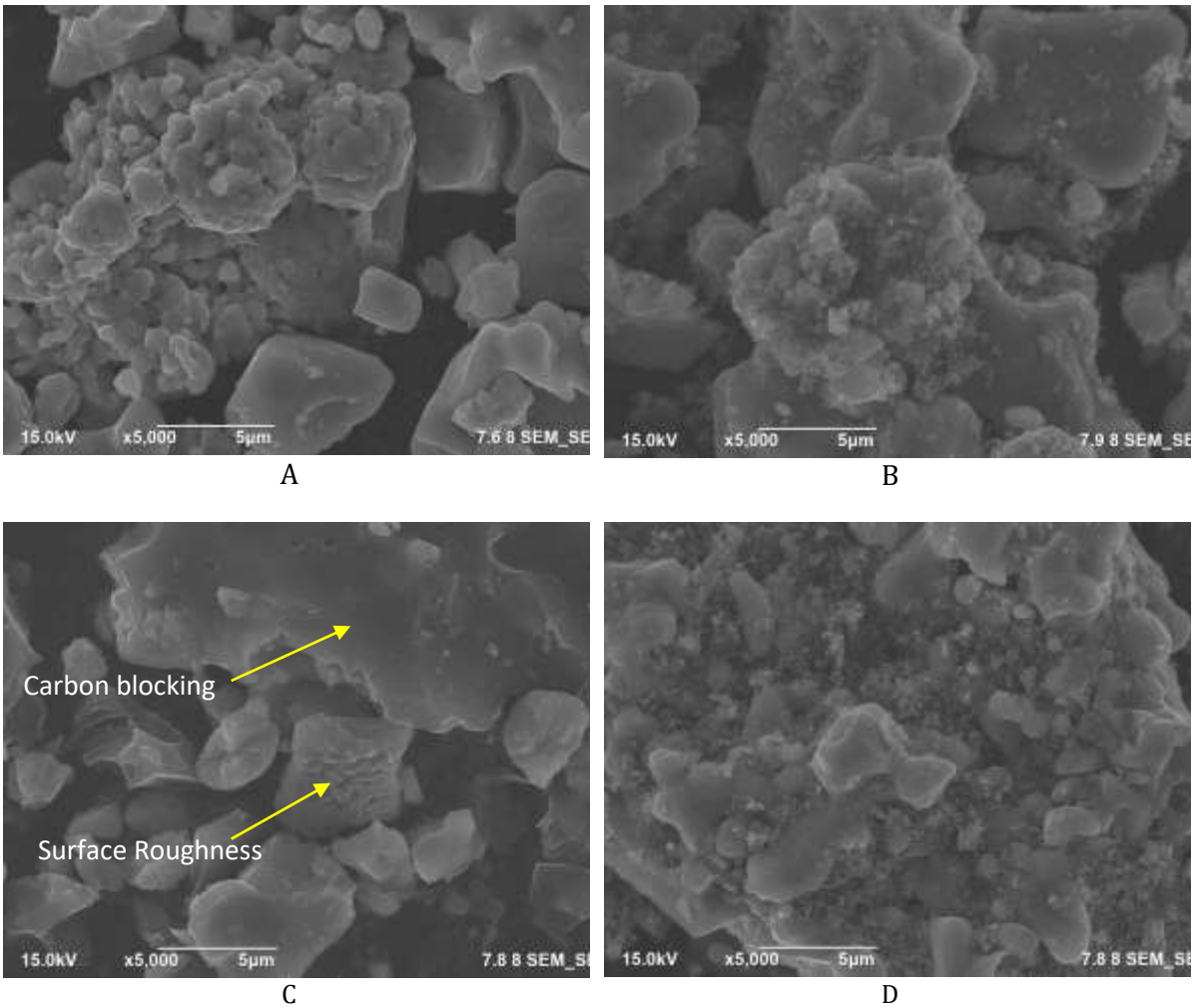

A B C D

Figure 3. The FESEM images of: (A) Pure LTO, (B) LTO/SP, (C) LTO/Sugar, (D) LTO/SP+PVDF.

The surface morphology of LTO particles is depicted in Figure 3. The particles have irregular polyhedrons, with an average of 5-10 μm. Figure 3A shows that pure LTO possesses less porosity and forms agglomerated particles. These morphology features should affect the electrochemical performances because the pores on the material enhance electrolyte penetration [29]. The particles are considerably big, measuring more than 5 μm in size, and slightly coarse. Also, some necking between grains remains visible even after the second sintering process. In contrast,

Figure 3B shows that the LTO particles are surrounded by carbon from SP homogenously. Figure 3C shows that the carbon from sugar covers and induces partial blocking on the LTO surface. This blocking should prevent electrolytes from entering the LTO, leading to a decreased capacity. It could be from a pyrolysis product at low temperatures that still contains hydrocarbon species such as hydrogen, nitrogen, volatile and ash [30, 31]. Nevertheless, the carbon coating feature of sugar is the formation of surface roughness on the morphology, as depicted in Figure 3C, essential in the electrochemical process [19]. The roughness increases the surface contact between LTO and electrolyte, resulting in higher capacity [32]. Figure 3D shows that SP surrounds the LTO particles covered by the carbon coating generated by the pyrolysis of PVDF at 600°C. This additional carbon coating significantly affects the electrochemical performances of LTO.

3.2 Cross-section of Electrodes

Figure 4 shows the FESEM micrographs of the cross-section of electrode, displaying two layers of active materials on the top layer and a copper base on the bottom layer. The active material layers have a thickness of about 50 to 70 μm. The carbon coating in samples of Pure LTO, LTO/SP, and LTO/SP+PVDF are relatively homogenous, while the carbon from SP mixes with other samples. Furthermore, the carbon from sugar in LTO/sugar sample is gathered close to the surface of the active material. This gathered carbon prevents the penetration of electrolytes into the active materials. Nevertheless, sugar carbon increases the bonding between the active material and copper foil as a current collector because the rough material enhances their contact area [29].

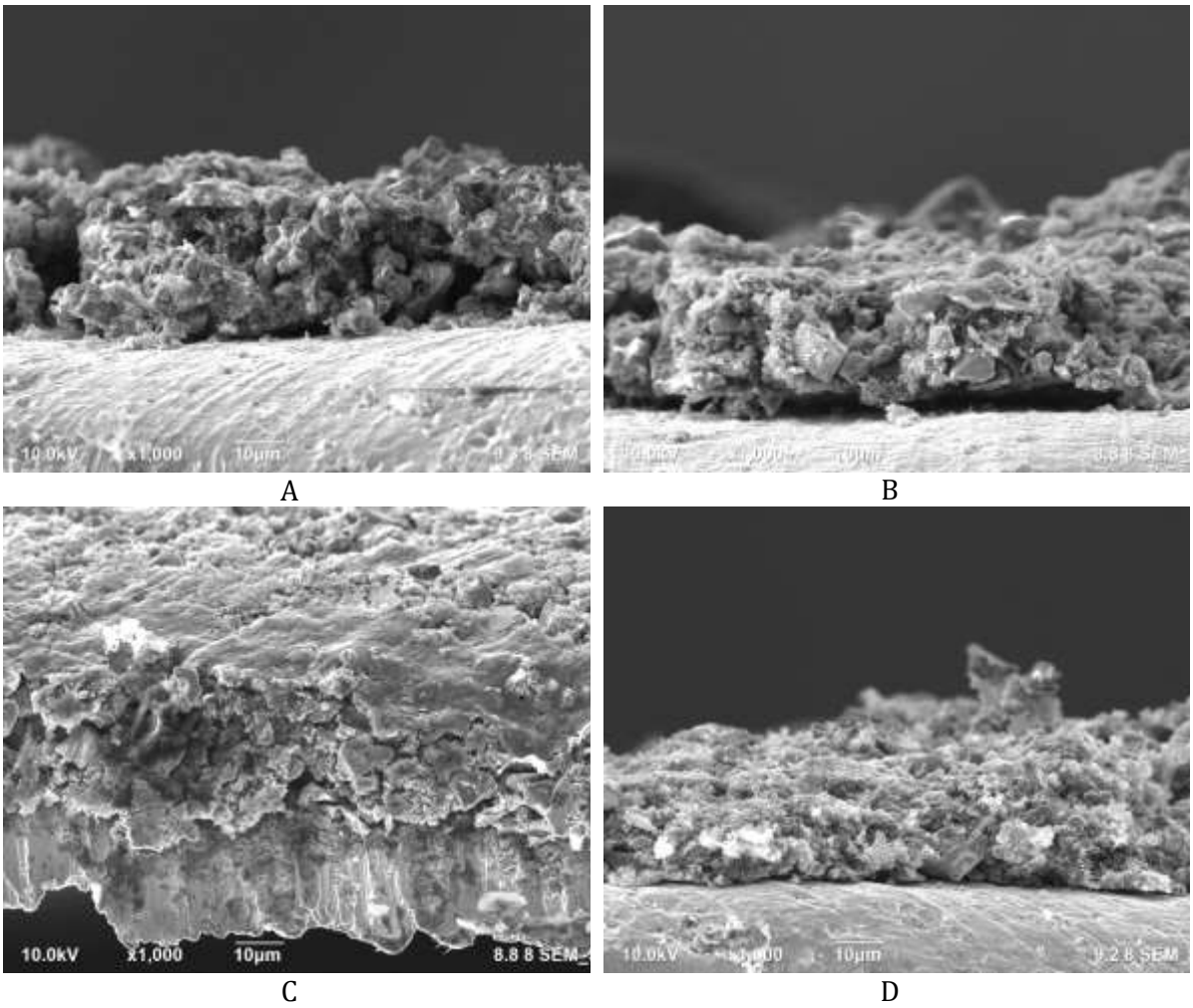

Figure 4. The FESEM images of electrode sheet cross-section of: (A) Pure LTO, (B) LTO/SP, (C) LTO/Sugar, (D) LTO/SP+PVDF.

3.3 FTIR Spectra of Particles

FTIR spectra in Figure 5 show that each sample has two absorption peaks at 650 and 470 cm^{-1} related to Ti-O symmetry and asymmetry stretching vibration. These peaks are fingerprints or characteristics of the octahedral structure of LTO [33]. Additionally, the FTIR data confirms that samples C and D have peaks at 1500 cm^{-1} corresponding to –NH stretching, while peaks at 3400 cm^{-1} were associated with O-H stretching [34]. This additional content affects the electrochemical performance of cell battery such as specific capacity, rate capability and cycling performance.

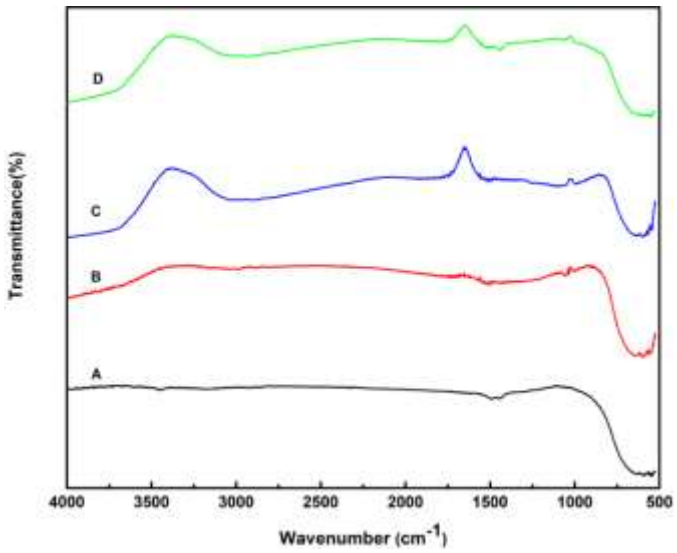

Figure 5. FTIR spectra of: (A) Pure LTO, (B) LTO/SP, (C) LTO/Sugar, (D) LTO/SP+PVDF.

3.4 EIS Spectra

Figure 6 shows the electrochemical impedance spectroscopy (EIS) evaluation results conducted in the range frequencies from 100 kHz to 0.1 Hz to understand the effect of carbon coating on the samples' electrical conductivity. All curves comprise a semicircle at high frequency and a tilted line at low frequency. The internal resistance (Rs) caused by the electrolyte's resistance was determined using the intersection of the semicircle at the lower frequency region. In contrast, the charge transfer resistance (Rct) was derived from semicircle diameter at the middle-frequency region [35]. The tilted line at the lower frequency region could be attributed to the Warburg diffusion [36]. The samples with a carbon coating have relatively lower resistivity than pure LTO, indicating that the carbon coating could increase conductivity. The sample of LTO/SP has a lower diameter, implying a lower charge transfer impedance or higher electronic conductivity than other samples [37]. SP carbon with porous characteristics allows the electrolyte to penetrate the sample. However, the sample of LTO/SP+PVDF lacks the tilted line, indicating difficulty in Li diffusion. However, when sugar is used as a carbon source, it gives the highest charge transfer resistivity. Carbon from sugar blocked the electrode's pore, avoiding the electrolyte's penetration into the LTO as shown in Figure 3C. Table 2 shows that Rs values decrease after carbon coating, while Rct values vary greatly.

Table 2 Data acquired after fitting and analysis using Zview

Sample	$Rs=R_1$ (Ω)	R_2 (Ω)	$Rct=R_2-R_1$ (Ω)	R_3	CPE1	CPE2	W
Pure LTO	5.66	198.3	192.64	46.11	0.74	4.87	0.52
LTO/SP	4.55	77.69	73.14	9.71	0.72	4.02	0.39
LTO/Sugar	3.49	225.1	221.61	16.21	0.81	4.37	0.38
LTO/SP+PVDF	2.54	185.30	182.85	138	0.66	4.66	0.71

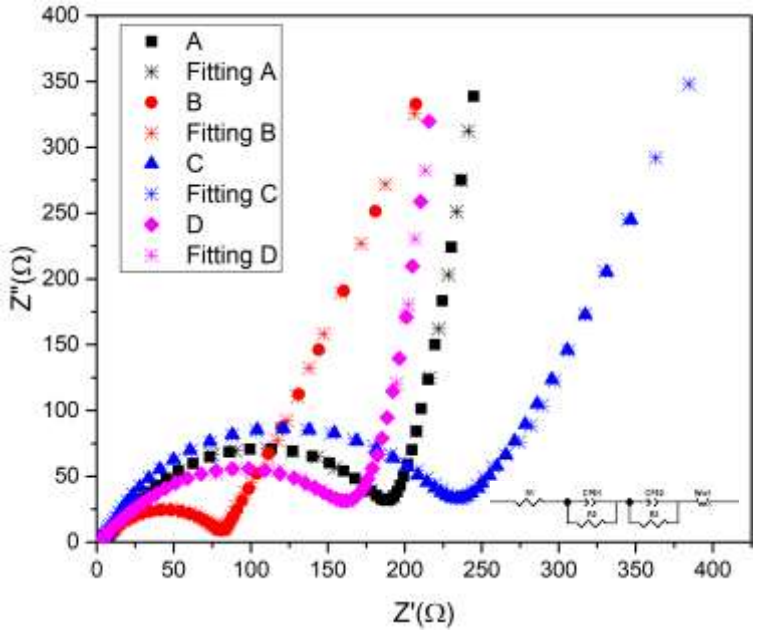

Figure 6. Nyquist plots of: (A) Pure LTO, (B) LTO/SP, (C) LTO/Sugar, (D) LTO/SP+PVDF.

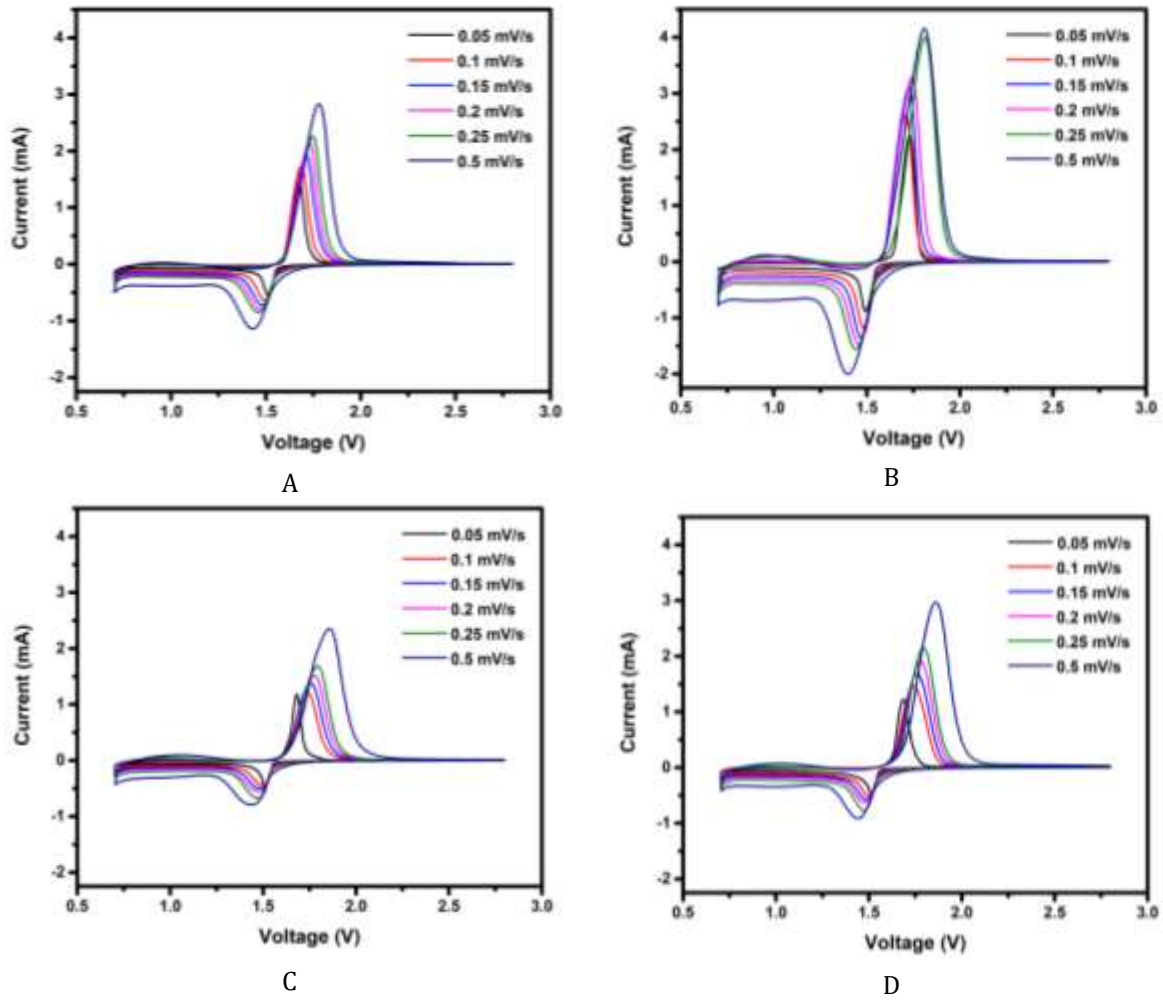

Figure 7. Cyclic voltammetry of: (A) Pure LTO, (B) LTO/SP, (C) LTO/Sugar, (D) LTO/SP+PVDF at different scan rates (0.05, 0.1, 0.15, 0.2, 0.25, and 0.5 mVs^{-1}).

3.5 Cyclic Voltammetry (CV)

Figure 7 shows the CV testing results at various scan rate conducted to investigate the electrochemical performances. Six pairs of oxidation and reduction peaks correspond to the Ti^{4+}/Ti^{3+} redox couple of LTO. There is no signal from rutile at the CV curve since rutile is thermodynamically stable, and it could only be inserted by Li-ion when the particle size is less than 20 nm. Moreover, the potential difference between anodic and cathodic peaks indicates the polarization of materials. Increasing scan rate shifts the oxidation peaks to the right and the reduction peak shifts to the left due to the polarization. The samples of LTO/SP and pure LTO show the lowest and the highest polarization with a potential range of 0.4089 V and 0.4378 V, respectively. In contrast, the samples of LTO/Sugar and LTO/SP+PVDF have a polarization of 0.4208 V and 0.4166 V, respectively. The polarization data shows that carbon coating decreases the polarization. Therefore, the lower sample polarization increases the reversibility of the redox reaction.

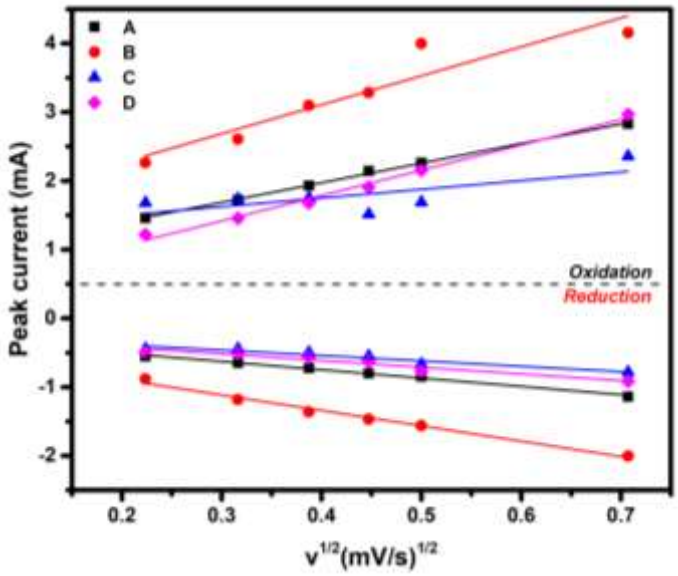

Figure 8. The relationship between Ip and v1/2 acquired from CV curves of: (A) Pure LTO, (B) LTO/SP, (C) LTO/Sugar, (D) LTO/SP+PVDF.

Table 3 The coefficient of sample lithium-ion diffusion

	Pure LTO	**LTO/SP**	**LTO/Sugar**	**LTO/SP+PVDF**
$\mathbf{D_{eoxidation}}$	1.4×10^{-10}	3.4×10^{-10}	9.79×10^{-11}	1.25×10^{-10}
$\mathbf{D_{reduction}}$	2.05×10^{-11}	6.62×10^{-11}	1.04×10^{-11}	1.38×10^{-11}

Figure 8 shows the relationship between current peaks and the square root of the scan rate for oxidation and reduction peaks. The linear curves indicate the diffusion of lithium-ion during insertion and extraction. The lithium-ion diffusion coefficient is calculated using the Randles-Sevcik equation upon the relationship between the redox peak and the square root of the scan rate [38]:

$$i_p = 0.4463\, nFAC \left(\frac{nFvD}{RT}\right)^{1/2} \quad (2)$$

where n =3 is the number of electrons in the redox reaction, A is the electrode surface area (cm^2), while C is the molar concentration of lithium ions (0.00437 $mol.cm^{-3}$), D is the diffusion coefficient of lithium ions and v is the scan rate of the potential ($V.s^{-1}$). Table 3 shows that carbon coating using super-P increases the lithium-ion diffusion more than sugar coating. Additionally, carbon coating using SP+PVDF is less effective than the other method.

3.6 Capacity Measurement

The effect of different carbon coating was determined by the charge-discharge curves for all using constant-current (CC) technique with different currents within the potential range of 0 – 3.0 V shown in Figure 9. The CD curves form a flat potential plateau at 1.55 V assigned to the insertion reaction between LTO and $Li_7Ti_5O_{12}$. In contrast, the potential plateau at 0.8 V could be ascribed to the insertion reaction between $Li_7Ti_5O_{12}$ and $Li_9Ti_5O_{12}$. Figure 9 shows that the charge-discharge curves are similar for uncoated and coated samples, indicating that the carbon coating does not alter the basic spinel structure [39]. The specific capacities are higher than theoretical (175 $mAhg^{-1}$) because they were discharged to 0 V. The specific capacities of each sample

decreased as the scan rate increased, followed by the degradation of the working voltage and the enhancement of the discharge plateau slant.

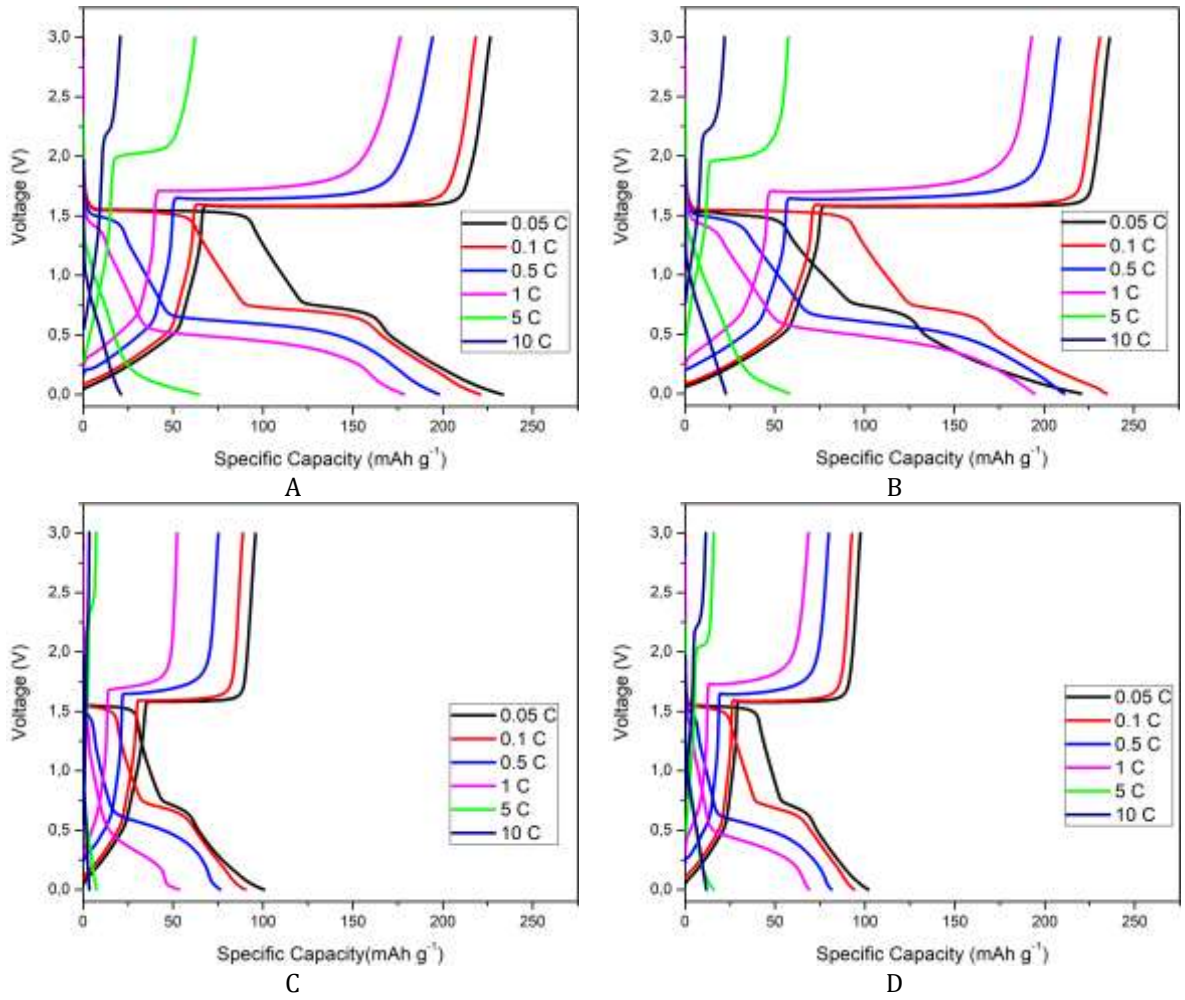

Figure 9. Charge and discharge curves for samples at different rates of: (A) Pure LTO, (B) LTO/SP, (C) LTO/Sugar, (D) LTO/SP+PVDF.

3.7 Rate Capability and Cycling Performance

The comparison of rate capability of samples at different current rates was also used to investigate the electrochemical performance, and it is displayed in Figure 10. The current density was increased gradually from 0.05C to 10 C and returned to 0.05C again. The cells were run for 5 cycles at each of the C rates. LTO/SP sample possesses better rate capability for all C-rate than other samples, suggesting that the addition of super P into LTO could improve cycling performance. Furthermore, it has a better specific capacity than Pure LTO at a high charge-discharge rate, meaning it has a higher power density. The rate capability of LTO/Sugar sample significantly decreased because carbon from sugar lacks a porous structure as shown in Figure 4C. Meanwhile, LTO/SP+PVDF sample possesses lower rate capability than pure LTP since the carbon from PVDF enclosed the pore of super P under high-temperature sintering.

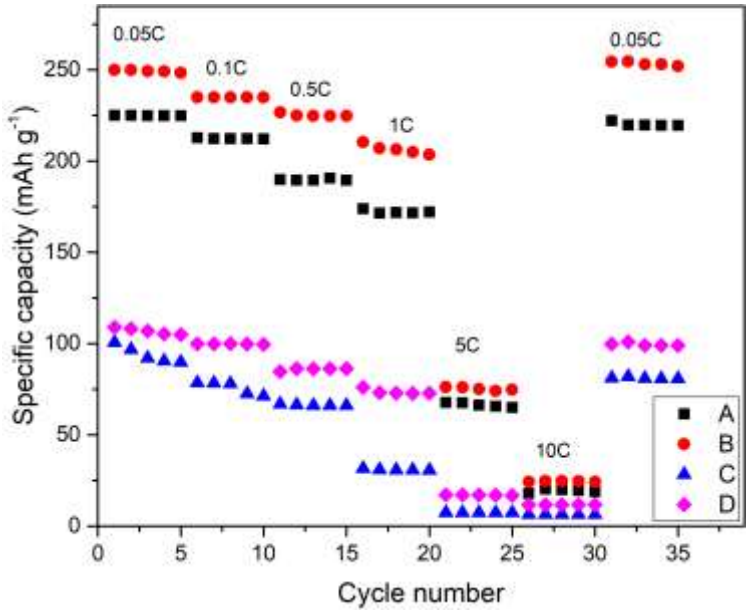

Figure 10. Rate capability of: (A) Pure LTO, (B) LTO/SP, (C) LTO/Sugar, (D) LTO/SP+PVDF.

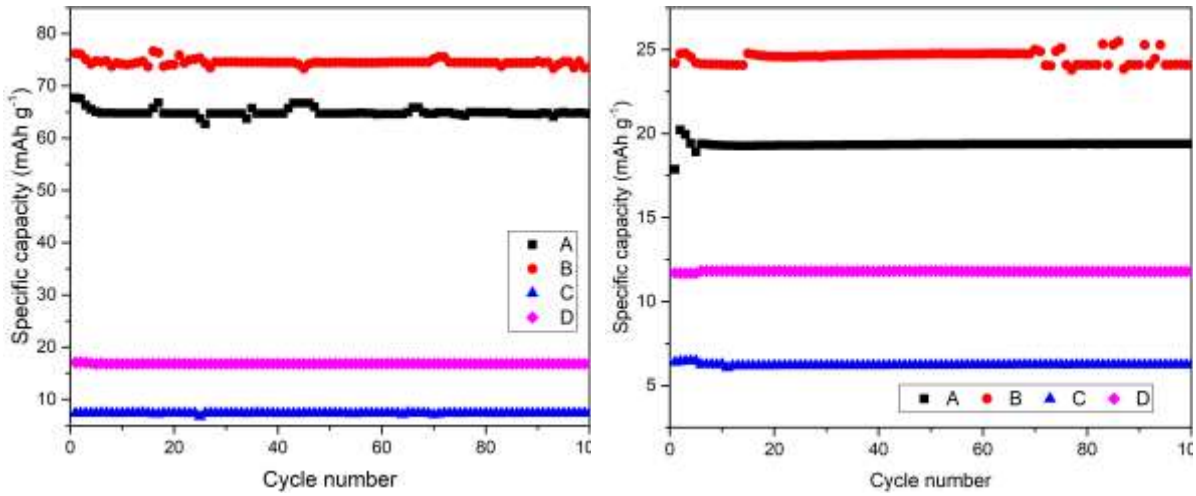

Figure 11. Cycling performance of: (A) Pure LTO, (B) LTO/SP, (C) LTO/Sugar, (D) LTO/SP+PVDF at (left) 5 C and (right) 10 C for 100 cycles.

Figure 11 shows the cycling performance of the four samples at 5C (left) and 10 C (right) for 100 cycles respectively. Despite unstable cycling performance, LTO/SP sample still achieves the highest specific capacity. Considering this result, it is believed that the contribution of super P to the enhancement of conductivity cannot be neglected. LTO/Sugar sample shows inferior performance since carbon from sugar blockade the particle and prevent the penetration of electrolyte. From the FTIR spectra, both LTO/Sugar and LTO/SP+PVDF have -OH and -NH_3 bond on the surface of LTO, this impurity makes less active of the electrolyte. The cycling performance indicates that carbon super P enhance the electrochemical performance especially for high C-rate.

4. CONCLUSION

Carbon-coated LTO are successfully prepared using the Sol-Gel process from different sources and methods. XRD patterns for Pure LTO and carbon-coated LTO are similar, meaning that carbon coating does not significantly change the LTO phase during coating. The FESEM images show that particles have various sizes, and the sugar carbon blocked the electrode sheet surface pores. Furthermore, the LTO sample coated by Super P had the best specific capacity because carbon coating increases conductivity. Therefore, carbon coating using super P elevates LTO's reversibility. The ability of carbon-coated LTO to deliver high charge-discharge current indicated that they could be used for high-power energy storage applications.

ACKNOWLEDGEMENTS

This work was funded by the Research Grant of PUTI Doctor 2021 from Universitas Indonesia.

REFERENCES

[1] Yu, X., Pan, H., Wan, W., Ma, C., Bai, J., Meng, Q., Ehrlich, S., Hu, Y., Yang, X., Nano Lett. vol **13**, issue 10 (2013) pp. 4721-4727.
[2] Wang, J., Li, Y., Zhang, X., Deng, H., Zhao, Y., Cheng, Q., Gao, Xu., Tang, S., Cao, Y., Results Phys. vol **13**, (2019) pp. 1-3.
[3] Yan, L., Qian, S., Yu, H., Li, P., Lan, H., Long, N., Zhang, R., Shui, M., Shu, J., ACS Sustainable Chem. Eng. vol **5**, issue 1 (2017) pp. 957-964.
[4] Yan, B., Li, M., Bai, Z., Yang, J., Xiong, D., Li, D., et al., J. Mater. Chem. A. vol **3**, issue 22 (2015) pp. 11773-11781.
[5] Chung, Y., Shin, Y., Liu, Y., Park, J., Margez, C., Greszler, T., J. Electroanal. Chem. vol **837**, (2019) pp. 240-245.
[6] Yuan, T., Tan, Z., Ma, C., Yang, J., Ma, Z., Zheng, S., Adv. Energy Mater. vol **7**, issue 12 (2017) p. 1601625.
[7] Yang, X., Huang, Y., Wang, X., Jia, D., Pang, W., Guo, Z., Tang, X., J. Power Sources. Vol 257, (2014) pp. 280-285
[8] Huang, S., Wen, Z., Zhang, J., Gu, Z., Xu. X., Solid State Ionics. Vol 177, (2006) pp 851-855
[9] Shen, L., Li, H., Uchaker, E., Zhang. X., Cao, G., Nano Lett. Vol 12, (2012) pp. 5673-5678
[10] Pelegov, D., Koshkina, A., Pryakhina, V., Gorshkov, V., J. Electrochem. Soc. vol **166**, issue 3 (2019) pp. A5019-A5024.
[11] Qin, Q., Li, Y., Lv, X., Nanomaterials. vol **7**, issue 6 (2017) p. 150.
[12] Li, X., Xu, J., Huang, P., Yang, W., Wang, Z., Wang, M., Huang, Y., Zhou, Y., Qu, M., Yu, Z., Lin, Y., Electrochim. Acta vol **190**, (2016) pp. 69-75.
[13] Nitta, N., Wu, F., Lee, J., Yushin, G., Materials Today vol **18**, issue 5 (2015) pp. 252-264.
[14] Yang, G., Park, S., Sci. Rep. vol **9**, (2019) p. 4774.
[15] Tang, B., Li, A., Tong, Y., Song, H., Chen, X., Zhou, J., Ma, Z., J. Alloys Compd. vol **708**, (2017) pp. 6-13.
[16] Guo, X., Xiang, H., Zhou, T., Electrochim. Acta, vol **109**, (2013) pp. 33-38.
[17] Cao, S., Feng, X., Song, Y., Xue, X., Liu, H., Miao, M., Fang, J., Shi, L., ACS Appl. Mater. Interfaces vol **7**, issue 20 (2015) pp. 10695-10701.
[18] An, D., Shen, L., Lei, D., Wang, L., Ye, H., Li, B., Kang, F., He, Y., J. Energy Chem. vol **31**, (2019) pp. 19-26.
[19] Nasara, R., Tsai, P., Lin, S., Adv. Mater. Interfaces vol **4**, issue 15 (2017) p. 1700329.
[20] Zhang, H., Deng, Q., Mou, C., Huang, Z., Wang, Y., Zhou, A., Li, J., J. Power Sources vol **239**, (2013) pp. 538-545.
[21] Zhao, B., Ran, R., Liu, M., Shao, Z., Mater. Sci. Eng. R Rep. vol **98**, (2015) pp. 1-71.
[22] Chen, Z., Li, H., Wu, L., Lu, X., Zhang, X., Chem. Rec. vol **18**, issue 3 (2018) pp. 350-380.

[23] Sun, X., Radovanovic, P., Cui, B., New J. Chem. vol **39**, issue 1 (2015) pp. 38-63.
[24] Wang, Y., Liu, H., Wang, K., Eiji, H., Wang, Y., Zhou, H., J. Mater. Chem. vol **19**, issue 37 (2009) pp. 6789-6795.
[25] Yang, L., Li, H., Liu, J., Lu, Y., Li, S., Min, J., Yan, N., Men, Z., Lei, M., J. Alloys Compd. vol **689**, (2016) pp. 812-819.
[26] Wang, Y., Gu, L., Guo, Y., Li, H., He, X., Tsukimoto, S., Ikuhara, Y., Wan, L., J. Am. Chem. Soc. vol **134**, issue 18 (2012) pp. 7874-7879.
[27] Zhu, Z., Cheng, F., Chen, J., J. Mater. Chem. A. vol **1**, issue 33 (2013) pp. 9484-9490.
[28] Deng, H., Liang, W., Nie, D., Wang, J., Gao, X., Tang, S., Liu, C., Cao, Y., J. Nanomater. vol 2018, (2018) pp. 1-6.
[29] Sun, B., Wang, R., Ni, L., Qiu, S., Zhang, Z., Inorg. Chem. Commun. vol **93**, (2018) pp. 10-14.
[30] Bulut, A., Karagöz, S., Sci. World J. vol 2013, (2013) pp. 1-3.
[31] Destyorini, F., Yudianti, R., Irmawati, Y., Hardiansyah, A., Hsu, Y., Uyama, H., Diamond Relat. Mater. vol **117**, (2021) p. 108443.
[32] Shen, X., Shao, L., Tian, Z., Hu, Z., Cao, G., Int. J. Electrochem. Sci. vol **15**, (2020) pp. 9013-9023.
[33] Xue, B., Wang, K., Tan, Y., Li, Q., Sun, J., Ionics vol **25**, issue 6 (2019) pp. 2535-2542.
[34] Hong, S., Lee, S., Joo, O., Kang, J., Cho, B., Lim, J., J. Mater. Sci. vol **51**, issue 13 (2016) pp. 6220-6234.
[35] Kuo, Y., Lin, J., Electrochim. Acta vol **142**, (2014) pp. 43-50.
[36] Wu, K., Yang, J., Qiu, X., Xu, J., Zhang, Q., Jin, J., Zhuang., Electrochim. Acta vol **108**, (2013) pp. 841-851.
[37] Li, D., Zhao, W., Gao, Y., Cao, L., Qi, T., J. Electroanal. Chem. vol **851**, (2019) p. 113441.
[38] Krajewski, M., Hamankiewicz, B., Michalska, M., Andrzejczuk, M., Lipinska, L., Czerwinski, A., RSC Adv. vol **7**, issue 82 (2017) pp. 52151-52164.
[39] Yi, T., Liu, H., Zhu, Y., Jiang, J., Xie, Y., Zhu, R., J. Power Sources vol **215**, (2012) pp. 258-265.